

Stabilization of Hypersonic Boundary Layers by Linear and Nonlinear Optimal Perturbations

Pedro Paredes,^{*} Meelan M. Choudhari,[†] and Fei Li[‡]

NASA Langley Research Center, Hampton, VA 23681

The effect of stationary, finite-amplitude, linear and nonlinear optimal perturbations on the modal disturbance growth in a Mach 6 axisymmetric flow over a 7° half-angle cone with 0.126 mm nose radius and 0.305 m length is investigated. The freestream parameters ($M = 6$, $Re' = 18 \times 10^6/\text{m}$) are selected to match the flow conditions of a previous experiment in the VKI H3 hypersonic tunnel. Plane-marching parabolized stability equations are used in conjunction with a partial-differential equation based planar eigenvalue analysis to characterize the boundary layer instability in the presence of azimuthally periodic streaks. The streaks are observed to stabilize nominally planar Mack mode instabilities, although oblique Mack mode and first-mode disturbances are destabilized. Experimentally measured transition onset in the absence of any streaks correlates with an amplification factor of $N = 6$ for the planar Mack modes. For high enough streak amplitudes, the transition threshold of $N = 6$ is not reached by the Mack mode instabilities within the length of the cone; however, subharmonic first-mode instabilities, which are destabilized by the presence of the streaks, do reach $N = 6$ near the end of the cone. The highest stabilization is observed at streak amplitudes of approximately 20 percent of the freestream velocity. Because the use of initial disturbance profiles based on linear optimal growth theory may yield suboptimal control in the context of nonlinear streaks, the computational predictions are extended to nonlinear optimal growth theory. Results show that by using nonlinearly optimal perturbation leads to slightly enhanced stabilization of plane Mack mode disturbances as well as reduced destabilization of subharmonic first-mode disturbances.

Nomenclature

A	streak amplitude parameter	T	temperature
As_u	streak amplitude based on streamwise velocity	T_w	wall temperature
E	energy norm	(u, v, w)	streamwise, wall-normal and spanwise velocity components
G	energy gain	(x, y, z)	Cartesian coordinates
h_1	streamwise metric factor	α	streamwise wavenumber
h_3	spanwise metric factor	β	spanwise wavenumber
J	objective function	δ	similarity scale
L	cone length	κ	streamwise curvature
m	azimuthal wavenumber	ω	angular frequency
M	Mach number	ρ	density
$\bar{\mathbf{q}}$	vector of base flow variables	θ	local half-angle
$\tilde{\mathbf{q}}$	vector of perturbation variables	ν	kinematic viscosity
$\hat{\mathbf{q}}$	vector of amplitude variables	(ξ, η, ζ)	streamwise, wall-normal and spanwise coordinates
Re	Reynolds number	$\mathbf{A}, \mathbf{B}, \mathbf{C}, \mathbf{D}, \mathbf{L}$	PSE matrix operators
r_b	local radius	$\mathbf{P}, \mathbf{Q}, \mathbf{R}, \mathbf{S}, \mathbf{T}, \mathbf{V}$	plane-marching PSE matrix
r_n	nose radius		

^{*}NASA NPP Fellow, Computational AeroSciences Branch. AIAA Member

[†]Research Scientist, Computational AeroSciences Branch. AIAA Associate Fellow

[‡]Research Scientist, Computational AeroSciences Branch.

	operators	DA	discrete adjoint
F	nonlinear vector operator	EVP	eigenvalue problem
M	energy weight matrix	FM	first mode
<i>Subscript</i>		FST	freestream turbulence
<i>lin</i>	linear	L	linear
<i>mean</i>	mean gain	LST	linear stability theory
<i>out</i>	outlet gain	MFD	mean flow distortion
∞	freestream value	MM	Mack mode
0	initial position	MVG	micro vortex generators
1	final position	NL	nonlinear
<i>Superscripts</i>		NS	Navier-Stokes
*	dimensional value	OSE	Orr-Sommerfeld and Squire equations
<i>H</i>	conjugate transpose	PDE	partial differential equations
<i>Abbreviations</i>		PSE	parabolized stability equations
CA	continuous adjoint	TS	Tollmien-Schlichting

I. Introduction

Laminar-turbulent transition of boundary layer flows can have a strong impact on the performance of hypersonic vehicles because of its influence on the surface skin friction and aerodynamic heating. Therefore, the prediction and control of transition onset and the associated variation in aerothermodynamic parameters in high-speed flows is a key issue for optimizing the performance of the next-generation aerospace vehicles.

Under low levels of background disturbances, transition is initiated by the exponential amplification of linearly unstable eigenmodes, i.e., modal instabilities of the laminar boundary layer. In two-dimensional boundary layers, different instability mechanisms dominate the exponential growth phase depending on the flight speed. Planar, i.e., two-dimensional, Tollmien-Schlichting (TS) waves are the most unstable in the incompressible regime, whereas oblique first-mode instabilities correspond to the most amplified disturbances in supersonic boundary layers. The hypersonic regime is again dominated by the growth of planar acoustic waves of the second mode, i.e., Mack mode type.¹ In the presence of sufficiently strong external disturbances in the form of either freestream turbulence (FST) or three-dimensional wall roughness, streamwise streaks involving alternately low and high streamwise velocity have been observed to appear in incompressible boundary layers.² Further research in the incompressible regime has shown that high amplitude streaks can become unstable to shear layer instabilities that lead to a form of “bypass transition.”³ When the streak amplitudes are low enough to avoid these instabilities, i.e., when the background disturbance level is moderate, the streaks can actually reduce the growth of the TS waves as documented in both theoretical and experimental studies.^{4–6} The stabilizing effect of stationary streaks in low-speed boundary layers has been used in passive flow control strategies to demonstrate delayed onset of transition by using micro vortex generators (MVG) along the body surface.^{7,8}

Despite the numerous research efforts focused on tripping hypersonic boundary layer flows by using roughness elements, there have been a few experimental and numerical studies reporting a delay in transition under certain circumstances. Most of these studies used two-dimensional roughness elements. James⁹ used fin-stabilized hollow tube models in free flight with a screw-thread type of distributed two-dimensional roughness. He found that for a given freestream Mach number between the range of 2.8 to 7, there exists an optimum roughness height for transition delay. Fujii¹⁰ studied the effects of two-dimensional roughness by using a 5° half-angle sharp cone at a freestream Mach number of 7.1. He also observed transition delay for certain conditions when the wavelength of the wavy wall roughness was comparable to that of the Mack mode instabilities. More recently, Font et al.^{11,12} performed numerical and experimental studies, respectively, that were focused on the effect of two-dimensional surface roughness on the stability of a hypersonic boundary layer at a freestream Mach number of 6. The experiments¹¹ used a flared cone with strips of roughness in the Boeing/AFOSR Mach 6 Quiet Tunnel and supported the numerical predictions indicating a stabilizing influence on the amplification of Mack mode disturbances.¹² In particular, these studies showed that the most dominant Mack mode instability could be suppressed via judicious placement of the roughness elements along the surface of the cone. Among the limited experimental evidence of delayed transition in a hypersonic

boundary layer and in the presence of three-dimensional roughness elements is the study by Holloway & Sterrett,¹³ who used a single row of spherical roughness elements partially recessed within a flat plate model in the NASA Langley 20-inch Mach 6 tunnel. Data for multiple Mach numbers at the boundary layer edge were obtained by varying the plate mounting angle. They found that, for cases with the smallest roughness diameters, transition was delayed for Mach numbers larger than 3.7, which approximately corresponds to the lower bound for second-mode dominance over first-mode instabilities in a flat plate boundary layer at typical wind tunnel conditions. Therefore, their results are suggestive of stabilizing influence of roughness-induced streaks on Mack mode waves. When the roughness height becomes sufficiently large, the streaks can develop high-frequency instabilities that can lead to earlier transition¹⁴ as found by Holloway & Sterrett.¹³

Theoretical studies of the interaction between stationary disturbances and Mack mode instabilities in hypersonic boundary layers have been recently initiated. Li et al.¹⁵ studied the interaction of Goertler vortices with Mack mode instabilities on a flared cone, demonstrating a possible route to transition via this interaction. Li et al.¹⁶ studied the secondary instability of crossflow vortices in a hypersonic cone at angle of attack and found that nonlinearly saturated crossflow vortices destabilize the Mack modes. Also, after the completion of this work, the authors became aware of the recent publication by Ren et al.,¹⁷ who studied the stabilizing effect of weakly nonlinear suboptimal streaks and Goertler vortices on the planar first-mode and Mack mode instabilities. Ren et al.¹⁷ documented a slight reduction in the logarithmic amplification factor, i.e., N -factor, relative to the baseline, zero-streaks case for both a flat plate boundary layer with suboptimal streaks ($\Delta N \approx 0.2$) and a concave plate with Goertler vortices. Recently, Paredes et al.¹⁸ have demonstrated that finite-amplitude optimal streaks can substantially damp planar Mack mode instabilities in the hypersonic flow over a circular cone at zero angle of attack, although first-mode instabilities are destabilized.

The development of roughness-induced streaks is strongly dependent on the details of roughness element shape, height, and spanwise or azimuthal spacing. A conceptually simple model that can characterize as well as provide an upper bound on the transient algebraic growth and subsequent slow decay of boundary layer streaks due to arbitrary initial disturbances is the optimal growth theory; see Ref. 19 for a review. The transient growth arises as a result of the non-normality of disturbance equations, and the optimal growth theory seeks to maximize the disturbance growth between a selected pair of streamwise locations. Regardless of the flow Mach number, the disturbances experiencing the highest magnitude of transient growth have been found to be stationary streaks that arise from initial perturbations that correspond to streamwise vortices. The instabilities of optimal streaks with finite initial amplitudes in supersonic and hypersonic boundary layers has been addressed in recent work;^{20,21} however, the effect of lower amplitude, i.e., stable, or at most weakly unstable streaks, on the growth of Mack mode instabilities has not been studied as yet. The present work seeks to bridge this gap with the goal of developing a more thorough knowledge base for transition prediction in the presence of stationary streaks and potentially expand the range of available techniques for transition control at hypersonic edge Mach numbers.

To that end, we study the effect of a periodic array of finite-amplitude streaks on the dominant instability waves in axisymmetric or two-dimensional boundary layers at hypersonic Mach numbers, i.e., the Mack mode instabilities. Figure 1 shows a schematic of the flow configuration considered in this work. The geometry is a 7° half-angle circular cone with $r_n = 0.126$ mm nose radius and $L = 0.305$ m length. The freestream parameters ($M = 6$, $Re' = 18 \times 10^6/\text{m}$, $T_\infty^* = 60.98$ K) are selected to match the flow conditions of a previous experiment in the VKI H3 hypersonic tunnel.²² Experimental measurements and theoretical predictions based on quasiparallel, linear stability theory (LST) and the nonparallel, parabolized stability equations (PSE) have confirmed that laminar-turbulent transition in this flow is driven by the modal growth of planar Mack mode instabilities.²² The array of actuators shown in Fig. 1 is purely notional, as the analysis presented herein is based on boundary layer streaks resulting from the transient growth of an optimal initial perturbation.

II. Theory

This section introduces the methodologies used in this paper. First, the linear optimal growth theory based on the PSE is briefly discussed. This method is used to obtain the optimal perturbation that results in a maximum energy gain at a downstream position. Furthermore, a nonlinear optimal growth theory based on the plane-marching PSE is also introduced. Then, both the linear and nonlinear optimal perturbations are used as initial condition with a given finite amplitude for the parabolic integration of the stationary,

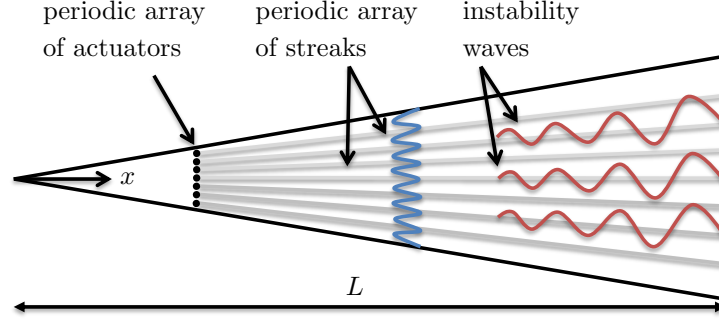


Figure 1. Sketch (side view) of the cone illustrating the present conceptual configuration. The wake of the periodic array of actuators generate the periodic array of streaks that modulate the instability waves.

nonlinear plane-marching PSE to obtain a three-dimensional, azimuthal-periodic, perturbed boundary layer flow. The modal instability analysis of the perturbed boundary layer flow is performed using the linear form of the plane-marching PSE, and its particularities are discussed here. Finally, the discretization and boundary conditions used in this paper are presented.

II.A. Linear optimal growth

Linear transient growth analysis is performed using the linear PSE as explained in Refs. 23 and 24. In the PSE context, the perturbations have the form

$$\tilde{\mathbf{q}}(\xi, \eta, \zeta, t) = \hat{\mathbf{q}}(\xi, \eta) \exp \left[i \left(\int_{\xi_0}^{\xi} \alpha(\xi') d\xi' + m\zeta - \omega t \right) \right] + \text{c.c.}, \quad (1)$$

where c.c. denotes complex conjugate. The suitably nondimensionalized, orthogonal, curvilinear coordinate system (ξ, η, ζ) denotes streamwise, wall-normal, and azimuthal coordinates and (u, v, w) represent the corresponding velocity components. Density and temperature are denoted by ρ and T . The Cartesian coordinates are represented by (x, y, z) . The vector of perturbation fluid variables is $\tilde{\mathbf{q}}(\xi, \eta, \zeta, t) = (\tilde{\rho}, \tilde{u}, \tilde{v}, \tilde{w}, \tilde{T})^T$, and the vector of amplitude functions is $\hat{\mathbf{q}}(\xi, \eta) = (\hat{\rho}, \hat{u}, \hat{v}, \hat{w}, \hat{T})^T$. The vector of basic state variables is $\bar{\mathbf{q}}(\xi, \eta) = (\bar{\rho}, \bar{u}, \bar{v}, \bar{w}, \bar{T})^T$. The streamwise and azimuthal wavenumbers are α and m , respectively; and ω is the angular frequency of the perturbation.

Upon introduction of the perturbation form, Eq. (1) into the linearized NS equation together with the assumption of a slow streamwise dependence of the basic state and the amplitude functions, thus neglecting the viscous derivatives in ξ , the PSE are recovered as follows

$$\mathbf{L}\hat{\mathbf{q}}(\xi, \eta) = \left(\mathbf{A} + \mathbf{B} \frac{\partial}{\partial \eta} + \mathbf{C} \frac{\partial^2}{\partial \eta^2} + \mathbf{D} \frac{1}{h_1} \frac{\partial}{\partial \xi} \right) \hat{\mathbf{q}}(\xi, \eta) = 0. \quad (2)$$

The linear operators \mathbf{A} , \mathbf{B} , \mathbf{C} , and \mathbf{D} are given by Pralits et al.²³ and h_1 is the metric factor associated with the streamwise curvature. The streamwise pressure gradient $\partial \hat{p} / \partial \xi$ in the streamwise momentum equation is dropped without any loss of accuracy for the present purely stationary disturbances of interest in this work as justified by Refs. 6 and 25.

The optimal initial disturbance, $\tilde{\mathbf{q}}_0$, is defined as the initial (i.e., inflow) condition at ξ_0 that yield a maximum objective function, $J(\tilde{\mathbf{q}})$. The objective function is defined as the energy gain of the perturbation up to a specified position, ξ_1 . We use two definition of the energy gain; namely, the outlet energy gain,

$$G_{out} = \frac{E(\xi_1)}{E(\xi_0)}, \quad (3)$$

and the mean energy gain,

$$G_{mean} = \frac{1}{\xi_1 - \xi_0} \frac{\int_{\xi_0}^{\xi_1} E(\xi') d\xi'}{E(\xi_0)}, \quad (4)$$

where E denotes the energy norm of $\tilde{\mathbf{q}}$. The energy norm is defined as

$$E(\xi) = \frac{1}{L_\zeta} \int_\zeta \int_\eta \tilde{\mathbf{q}}(\xi, \eta, \zeta)^H \mathbf{M} \tilde{\mathbf{q}}(\xi, \eta, \zeta) h_1 h_3 d\eta d\zeta, \quad (5)$$

where h_3 is the metric factor associated with the azimuthal curvature, \mathbf{M} is the energy weight matrix and the superscript H denotes conjugate transpose. The positive-definite energy norm used here was derived by Mack²⁶ and Hanifi et al.²⁷ and is defined as

$$\mathbf{M} = \text{diag} \left[\frac{\bar{T}(\xi, \eta)}{\gamma \bar{\rho}(\xi, \eta) M^2}, \bar{\rho}(\xi, \eta), \bar{\rho}(\xi, \eta), \bar{\rho}(\xi, \eta), \frac{\bar{\rho}(\xi, \eta)}{\gamma(\gamma - 1) \bar{T}(\xi, \eta) M^2} \right]. \quad (6)$$

The variational formulation of the problem to determine the maximum of the objective functional J leads to an optimality system,^{23,28,29} which is solved in an iterative manner starting from a random solution at ξ_0 that must satisfy the boundary conditions. Two approaches can be followed, the continuous adjoint (CA) followed by Pralits et al.²³ and Tumin & Reshotko²⁸ or the discrete adjoint (DA) followed by Zuccher et al.²⁹ for compressible boundary layers. The comparison of the results following both CA and DA provides a cross-validation of the transient growth module. Summarizing, the linear PSE, $\mathbf{L}\tilde{\mathbf{q}} = 0$, are used to integrate $\tilde{\mathbf{q}}$ up to ξ_1 , where the final optimality condition is used to obtain the initial condition for the backward continuous or discrete adjoint PSE integration. At ξ_0 , the adjoint solution is used to calculate the new initial condition for the forward PSE integration with the initial optimality condition. The iterative procedure finishes when the value of J has converged up to a certain tolerance, which was set to a relative error of 10^{-4} in the present computations.

II.B. Nonlinear optimal growth

Nonlinear transient growth analysis is performed using an implicit formulation of the nonlinear plane-marching PSE, which is equivalent to a perturbation form of the parabolized Navier-Stokes equations.^{20,30} In the nonlinear plane-marching PSE, the disturbance quantities are expanded in terms of their truncated Fourier expansion in time as

$$\tilde{\mathbf{q}}(\xi, \eta, \zeta, t) = \sum_{n=-N}^N \hat{\mathbf{q}}_n(\xi, \eta, \zeta) \exp \left[i \left(\int_{\xi_0}^{\xi} \alpha_n(\xi') d\xi' - n\omega t \right) \right] + \text{c.c.} \quad (7)$$

After substituting Eq. (7) into the NS equations, neglecting the viscous derivatives in ξ , and invoking the PSE assumptions, the plane-marching PSE can be written in a compact form as

$$\left(\mathbf{P}_n + \mathbf{Q}_n \frac{\partial}{\partial \eta} + \mathbf{R}_n \frac{\partial^2}{\partial \eta^2} + \mathbf{S}_n \frac{1}{h_3} \frac{\partial}{\partial \zeta} + \mathbf{T}_n \frac{1}{h_3^2} \frac{\partial^2}{\partial \zeta^2} + \mathbf{V}_n \frac{1}{h_1} \frac{\partial}{\partial \xi} \right) \hat{\mathbf{q}}_n(\xi, \eta, \zeta) = \mathbf{F}_n(\xi, \eta, \zeta) \exp \left(-i \int_{\xi_0}^{\xi} \alpha_n(\xi') d\xi' \right), \quad (8)$$

where \mathbf{F}_n is the Fourier component of the total forcing \mathbf{F} that arises from the nonlinear terms. The entries in the coefficient matrices \mathbf{P}_n , \mathbf{Q}_n , \mathbf{R}_n , \mathbf{S}_n , \mathbf{T}_n , \mathbf{V}_n and vector \mathbf{F} are found in Ref. 31. For the stationary disturbances of interest in this paper, $N = 0$ and $\alpha_0 = 0$.

The nonlinear optimization formulation follows the same procedure as the linear formulation, although in this case the initial perturbation is represented by two-dimensional amplitude function $\hat{\mathbf{q}}_0(\eta, \zeta)$. The energy gains are again defined as in Eqs. (3) and (4). As in the linear case, an optimality system is solved in an iterative manner starting from a random solution at ξ_0 . For the nonlinear computations, the linear optimal perturbation for the same set of parameters was used as initial condition with a selected finite amplitude. Summarizing, the nonlinear plane-marching PSE equations are used to integrate $\tilde{\mathbf{q}}$ up to ξ_1 , where the final optimality condition is used to obtain the initial condition for the backward continuous or discrete adjoint plane-marching PSE integration. The implicit integration of the forward problem is solved using a Newton iterative method at each streamwise position. Note that the adjoint equations remain linear for nonlinear optimization. At ξ_0 , the adjoint solution is used with the initial optimality condition to calculate the new initial condition for the forward nonlinear plane-marching PSE integration. The iterative procedure is stopped after the objective function is converged up to a specified tolerance, which was set to 10^{-4} as in the linear computations. Further details about the nonlinear optimization method can be found in Ref. 32.

II.C. Modal instability of perturbed flows

The linear, nonparallel stability characteristics of the modified basic state corresponding to the sum of the circular cone boundary layer and the finite-amplitude linear and nonlinear optimal disturbances is studied with the plane-marching PSE. The initial disturbance profiles for the plane-marching PSE are obtained using a partial-differential-equation (PDE) based two-dimensional eigenvalue problem (EVP). The linear form of the plane-marching PSE are recovered from Eq. (8) by setting $\mathbf{F} = 0$. A single nonstationary perturbation to the streak derived from Eq. (7) have the form

$$\tilde{\mathbf{q}}(\xi, \eta, \zeta, t) = \hat{\mathbf{q}}(\xi, \eta, \zeta) \exp \left[i \left(\int_{\xi_0}^{\xi} \alpha(\xi') d\xi' - \omega t \right) \right]. \quad (9)$$

The onset of laminar-turbulent transition is estimated using the logarithmic amplification ratio based on the energy norm E of Eq. (6),

$$N = - \int_{\xi_{lb}}^{\xi} \alpha_i(\xi') d\xi' + 1/2 \ln \left[\hat{E}(\xi) / \hat{E}(\xi_{lb}) \right], \quad (10)$$

relative to the location ξ_{lb} where the disturbance first becomes unstable. Accordingly, we assume that transition onset is likely to occur when the peak N -factor reaches a specified value.

II.D. Spatial discretization and boundary conditions

The PSE are integrated along the streamwise coordinate by using second-order backward differentiation. A constant step of $\Delta R = 2.5$, where $R = \sqrt{Re_x}$, along the streamwise direction is used. Finite differences^{33,34} (FD-q) of eighth-order are used for discretization of the wall-normal coordinate. In the transient growth computations with PSE, the wall-normal direction is discretized using $N_\eta = 201$. The nodes are clustered towards the wall.³⁴ The clustering of points is dependent on the boundary layer thickness, with half of the grid points located below $10 \times \delta$, where δ is the similarity scale. No-slip, isothermal boundary conditions are used at the wall, i.e., $\hat{u} = \hat{v} = \hat{w} = \hat{T} = 0$. The amplitude functions are forced to decay at the farfield boundary by imposing the Dirichlet conditions $\hat{p} = \hat{u} = \hat{w} = \hat{T} = 0$. The farfield boundary coordinate is set just below the shock layer.

The plane-marching PSE are used to predict the nonlinear evolution of finite-amplitude transient growth disturbances as well as the linear amplification characteristics of secondary instabilities sustained by those nonlinear disturbances. The plane-marching PSE are integrated using the same streamwise and wall-normal discretizations as that of the linear optimal growth analysis by using classic PSE. In addition to the streamwise and wall-normal directions, the azimuthal direction is discretized with Fourier collocation points. Note that the PSE operators of Eq. (2) depend only on the streamwise and wall-normal coordinates. Depending on the amplitude of the primary, optimal growth perturbation, the number of azimuthal points is varied from $N_\zeta = 16$ to $N_\zeta = 48$. Similar to the streamwise and wall-normal grids, the same azimuthal grids are used to compute the evolution of both finite-amplitude streaks and secondary modal disturbances.

The number of discretization points in all three directions was varied to ensure that the relevant flow quantities were insensitive to further improvement in grid resolution. Verification of the present linear optimal growth module against available transient growth results from the literature is shown in Refs. 35 and 24. Furthermore, the linear and nonlinear transient growth results are cross-validated by comparing continuous adjoint (CA) and discrete adjoint (DA) formulations.

III. Verification

The incompressible zero-pressure-gradient flat plate boundary layer flow is studied for verification of the nonlinear transient growth module. For this problem, the computational and physical coordinates coincide, i.e., $(\xi, \eta, \zeta) \equiv (x, y, z)$; and therefore, the metric terms are $h_1 = h_3 = 1$. Note that for the flat plate case, the azimuthal wavenumber m of the previously introduced perturbation forms, Eqs. (1) and (7), is substituted by an spanwise wavenumber β . To compare with the transient growth predictions based on the large Reynolds number asymptotic framework that leads to linearized boundary region equations,³⁶ the present transient growth results based on the PSE are computed using $Re_L = 10^8$ ($R_1 = 10,000$) to approximate asymptotic

predictions for a large Reynolds number, and $M = 10^{-3}$ to approximate incompressible conditions. The initial location is set at the leading edge $x_0 = 0$, and the final optimization location is set as reference length scale $x_1 = L$.

First, the linear transient growth predictions based on the continuous adjoint (CA) and the discrete adjoint (DA) approaches are compared for cross-validation purposes. The outlet energy gain G_{out} and the mean energy gain G_{mean} are selected as the objective functions to optimize. Figure 2(a) shows the optimal energy gains scaled with Re_L , i.e., G_{out}/Re_L and G_{mean}/Re_L , respectively, as functions of the spanwise wavenumber. The discrete and continuous adjoint approaches lead to indistinguishable predictions with both definitions of energy gain. By selecting the outlet energy gain G_{out} , the results of Andersson et al.³⁶ are recovered. The optimal spanwise wavenumber for maximum mean energy gain is approximately $\beta = 0.55$, which agrees with the prediction documented by Zuccher et al.³² of $\beta = 0.548$. Figure 2(b) shows the evolution of the energy norm scaled with Re_L by using the initial perturbations that yield maximum G_{out} and G_{mean} . The agreement between the predictions based on the discrete and continuous approaches is excellent.

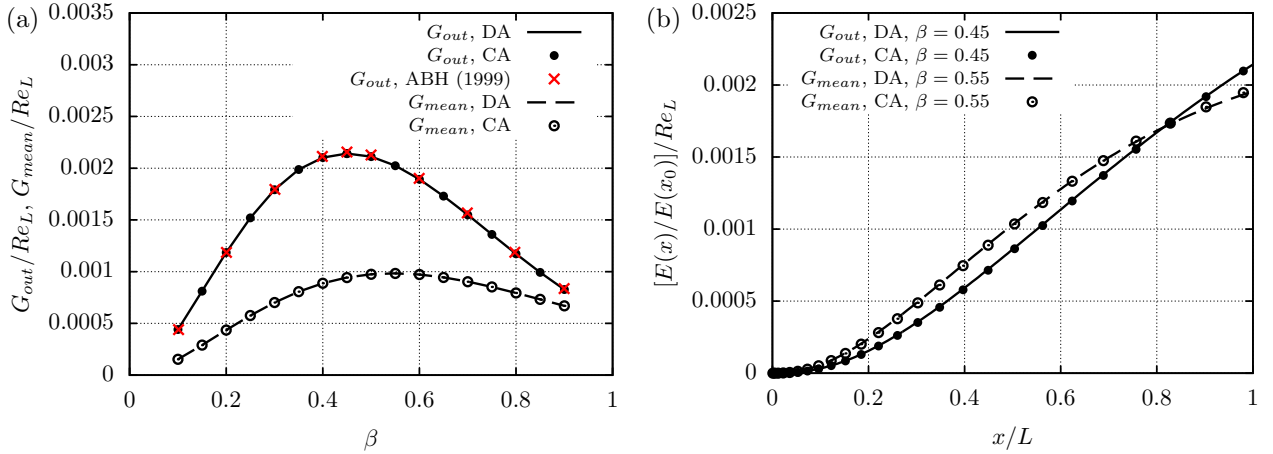


Figure 2. (a) Linear optimal outlet energy gain (G_{out}) and mean energy gain (G_{mean}) in the incompressible flat plate boundary layer with initial and final disturbance locations at $x_0 = 0$ and $x_1 = 1$. The results from Ref. 36 are denoted as ABH (1999). (b) Linear energy gain evolution with $\beta = 0.45$ for $J = G_{out}$ and $\beta = 0.55$ for $J = G_{mean}$. Results based on the continuous adjoint (CA) and the discrete adjoint (DA) approaches are included for comparison.

Finally, the nonlinear optimization module is validated using both discrete and continuous approaches with $J = G_{mean}$ and $\beta = 0.55$. Figure 3 shows the evolution of the energy norm ratio $[E(x)/E(x_0)]/Re_L$ with linear (L) and nonlinear (NL) optimal perturbations. The selected initial amplitudes ($A_0 = \sqrt{E_0}$) correspond to $E_0 = 10/Re_L$ and $E_0 = 25/Re_L$. The linear prediction is also shown. The nonlinear optimization achieves a slight increase of the energy gain for finite-amplitude perturbations. Again, the agreement between discrete and continuous adjoint formulations is excellent.

IV. Results

Next, we study the axisymmetric boundary layer over a 7° circular cone in Mach 6 free stream. The length of the nearly sharp cone is $L^* = 0.305$ m and the nose radius is $r_n^* = 0.126$ mm. The freestream conditions are selected to replicate those of a previous experiment in the VKI H3 hypersonic tunnel,²² i.e., Mach 6 flow at a unit Reynolds number of $18 \times 10^6/\text{m}$, and freestream temperature of $T_\infty^* = 60.98$ K. Freestream values are used as reference values for nondimensionalization. For this problem, the computational coordinates, (ξ, η, ζ) , are defined as an orthogonal body-fitted coordinate system. The metric factors are defined as

$$h_1 = 1 + \kappa\eta, \quad (11)$$

$$h_3 = r_b + \eta \cos(\theta), \quad (12)$$

where κ denotes the streamwise curvature, r_b is the local radius, and θ is the local half-angle along the axisymmetric surface, i.e., $\sin(\theta) = dr_b/d\xi$. For the present straight circular cone (with exception of the nose region that is not included in this analysis), $\kappa \equiv 0$ and θ is the half-angle of the cone equal to 7° .

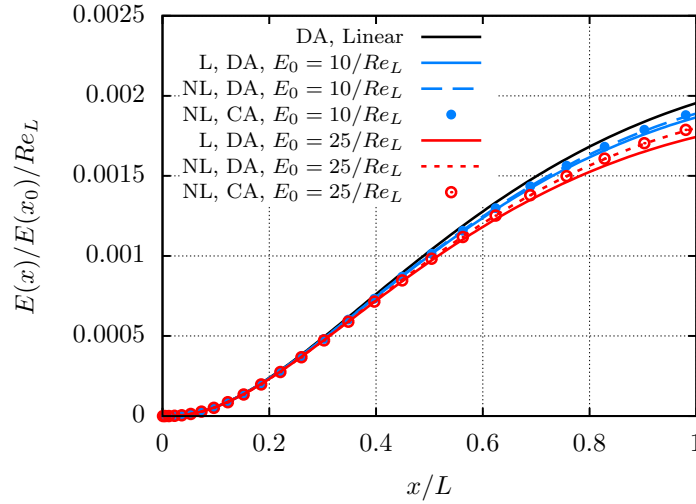


Figure 3. Evolution of energy ratio $E(x)/E(x_0)/Re_L$ of finite-amplitude, linear (L) and nonlinear (NL) optimal perturbations initialized at $x_0 = 0$ with $\beta = 0.55$ and $J = G_{mean}$. Results based on the continuous adjoint (CA) and on the discrete adjoint (DA) approaches are included for comparison. The linear prediction (Linear), which corresponds to an infinitesimal initial amplitude, is included.

IV.A. Transient growth characteristics

Herein, transient growth calculations are performed with the initial and final disturbance locations set to $x_0/L = 0.1957$ and $x_1/L = 0.4174$, respectively. The range $[x_0, x_1]$ has been chosen to obtain appreciable streak amplitudes over a majority of the cone length, as will be shown in what follows.

Linear transient growth predictions are presented first. Figure 4(a) shows the outlet energy gain G_{out} and the mean energy gain G_{mean} as a function of the azimuthal wavenumber. Again, the continuous and discrete adjoint approaches lead to equivalent results. The optimal azimuthal wavenumbers corresponding to maximum outlet and mean energy gains are found to be approximately equal to $m = 50$. Figure 4(b) shows the evolution of the energy norm ratio $E(x)/E(x_0)$ within the optimization domain $[x_0, x_1]$ for $m = 50$. As observed in the incompressible flat plate case in Fig. 2(b), the optimization of the mean energy gain yields a lower energy at x_1 than with the outlet energy gain selection; but the energy is larger within most of the integration domain. The components of the initial and final optimal perturbations with azimuthal wavenumber $m = 50$ and both energy gain selections, $J = G_{out}$ and $J = G_{mean}$, are plotted in Figs. 5(a) and 5(b), respectively. As previously observed for a hypersonic flow over a hemisphere,³⁷ using an objective function based on the mean energy gain (Fig. 5(b, left)) leads to optimum initial profiles with a slightly shorter wall-normal extension than the initial profiles obtained for an objective function based on the outlet energy gain (Fig. 5(a, left)). Furthermore, the peaks of the initial profiles in the former case are located slightly closer to the wall. The final perturbations are rather similar for both objective functions.

The nonlinear form of the plane-marching PSE is used to monitor the nonlinear development of the initial disturbances. Figure 6(a) shows the evolution of the streak amplitude based on \tilde{u} ,

$$As_u(\xi) = \frac{1}{2} [\max_{\eta, \zeta} (\tilde{u}(\xi, \eta, \zeta)) - \min_{\eta, \zeta} (\tilde{u}(\xi, \eta, \zeta))], \quad (13)$$

for selected amplitudes of the linear optimal inflow perturbation shown in Fig. 5(a) for $J = G_{out}$. Unlike the energy norm in Eq. (5), the velocity amplitude As_u is expected to be more closely related to the growth of streak instabilities. The streak amplitude parameter A corresponds to the maximum streak amplitude As_u achieved by a linear perturbation with the same initial amplitude, which is given by

$$A_0 = A \times \sqrt{E_{lin, A=1}}, \quad (14)$$

with $E_{lin, A=1}^* = 5.5516 \times 10^{-5} \text{ m} \cdot \text{Kg/s}^2$ for $J = G_{out}$ and $E_{lin, A=1}^* = 6.3513 \times 10^{-5} \text{ m} \cdot \text{Kg/s}^2$ for $J = G_{mean}$. As indicated by Eq. (14), the amplitude parameter A provides a convenient measure of the initial disturbance amplitude. As seen in Fig. 6(a), the nonlinear effects reduce the streak amplitude relative to the linear prediction; and hence, for any given case, $\max(As_u) < A$. This maximum moves progressively upstream as the amplitude parameter A is increased. Figures 6(b), 6(c) and 6(d) shows the isolines of streamwise

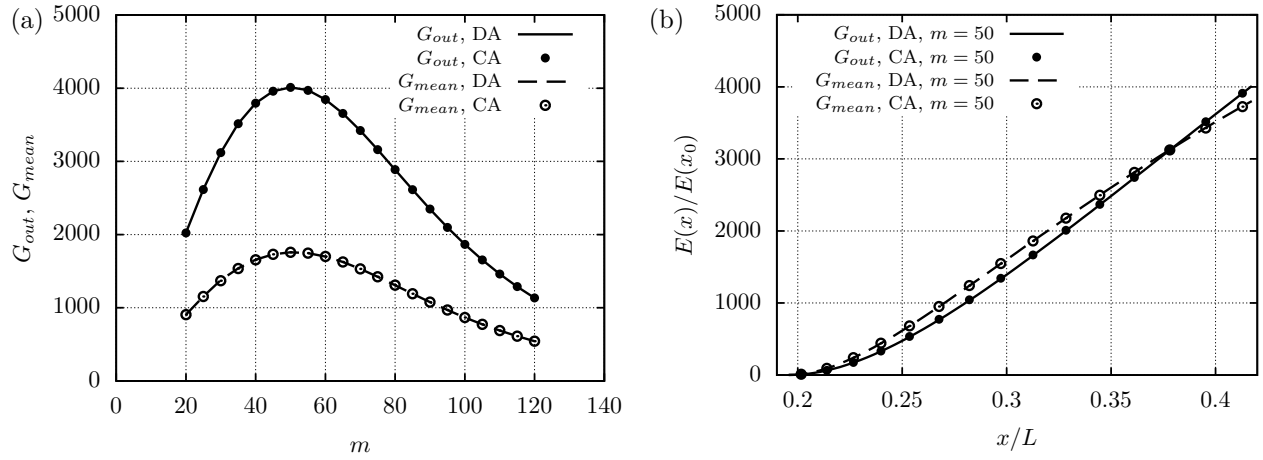


Figure 4. (a) Linear optimal outlet energy gain (G_{out}) and mean energy gain (G_{mean}) in the Mach 6 circular cone boundary layer with initial and final disturbance locations at $x_0/L = 0.1957$ and $x_1/L = 0.4174$. (b) Linear energy gain evolution with $m = 50$ for $J = G_{out}$ and $J = G_{mean}$. Results based on the continuous adjoint (CA) and on the discrete adjoint (DA) approaches are included for comparison.

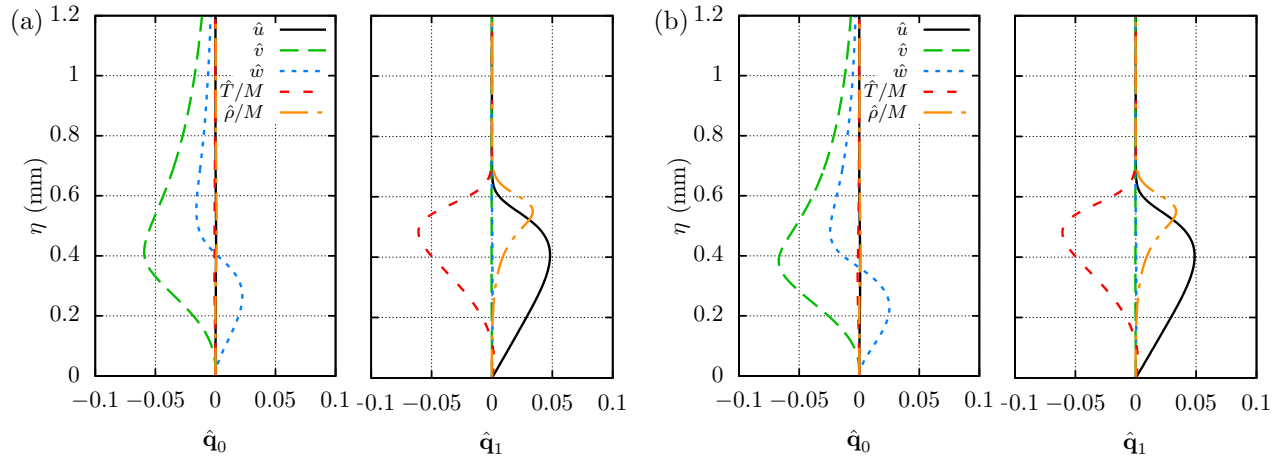


Figure 5. Initial and final amplitude vectors for (a) optimal outlet energy gain and (b) optimal mean energy gain, with $x_0/L = 0.1957$, $x_1/L = 0.4174$, and $m = 50$.

velocity component of the superposition of the basic state and the nonlinear perturbation in the crossplane at $x/L = 0.5$ for $A = 0.05$, $A = 0.10$ and $A = 0.20$, respectively. At the symmetry plane, $\zeta = L_\zeta/2$, the near-wall, low-momentum fluid is lifted upward by the counter-rotating vortices, resulting in a localized region of large boundary layer thickness and lower wall shear. At the lateral symmetry plane, $\zeta = 0$ (and $\zeta = L_\zeta/2$), the effect of the initial streamwise vortices is exactly the opposite, yielding a localized region of reduced boundary layer thickness and increased wall shear. As the streak amplitude is increased, the induced azimuthal gradients in the form of a detached three-dimensional shear-layer can support the growth of streak instabilities, as studied by Paredes et al.^{20,21}

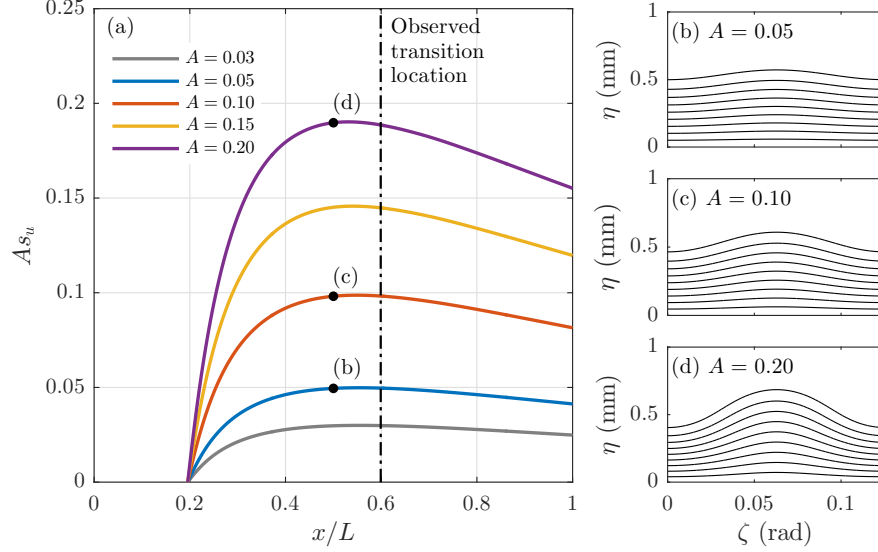


Figure 6. (a) Evolution of streak amplitudes based on u , As_u , of finite-amplitude, linear optimal perturbations initialized at $x_0/L = 0.1957$ with $m = 50$ and $J = G_{out}$. Also, isolines of streamwise velocity $\bar{u} = 0 : 0.1 : 0.9$, in the crossplane at $x/L = 0.5$ for (b) $A = 0.05$, (c) $A = 0.10$, and (d) $A = 0.20$.

Using initial disturbance profiles based on the linear optimal growth theory leads to somewhat suboptimal evolution of nonlinear streaks. Thus, nonlinear optimization is used with the objective function set equal to the mean energy gain, $J = G_{mean}$. Figure 7 shows the evolution of the streak amplitudes for linear and nonlinear optimal perturbations with $A = 0.10$ and $A = 0.20$ and the same optimization parameters used previously: $x_0/L = 0.1957$, $x_1/L = 0.4174$, and $m = 50$. Again, the discrete and continuous adjoint approaches lead to equivalent results. For these parameters, the nonlinear optimization yields a slight reduction in the peak value of streak amplitude. This result implies that an increase of energy norm is not necessarily equivalent to a higher value of streak amplitude.

IV.B. Modal instability characteristics of the unperturbed flow

Experimental measurements and theoretical predictions based on quasiparallel, linear stability theory (LST) and the nonparallel PSE have confirmed that laminar-turbulent transition in this flow is driven by the modal growth of planar Mack mode instabilities.²² The instability of the unperturbed flow is examined by PSE to establish the transition behavior in the absence of stationary streak perturbations. The onset of laminar-turbulent transition in the unperturbed boundary layer flow is estimated using N -factor evolution of the planar Mack modes computed with the PSE. For the conditions of the experiment,²² transition onset in the unperturbed cone boundary layer was measured to occur near $x/L = 0.6$. Figure 8 shows that the peak N -factor at the measured transition location corresponds to $N = 6$, which is reached by a planar Mack mode disturbance with frequency $F = 550$ kHz.

IV.C. Modal instability characteristics of the perturbed flow

The instability characteristics of the modified, streaky boundary layer flow are examined next. First, the streaks plotted in Fig. 6 corresponding to $J = G_{out}$ and finite-amplitude linearly optimal disturbances initiated at $x_0/L = 0.1957$ with $m = 50$ are studied. Figure 9 shows the frequency dependence of spatial growth rates at a fixed axial location of $x/L = 0.5$ as computed using quasiparallel PDE-based EVP. Results

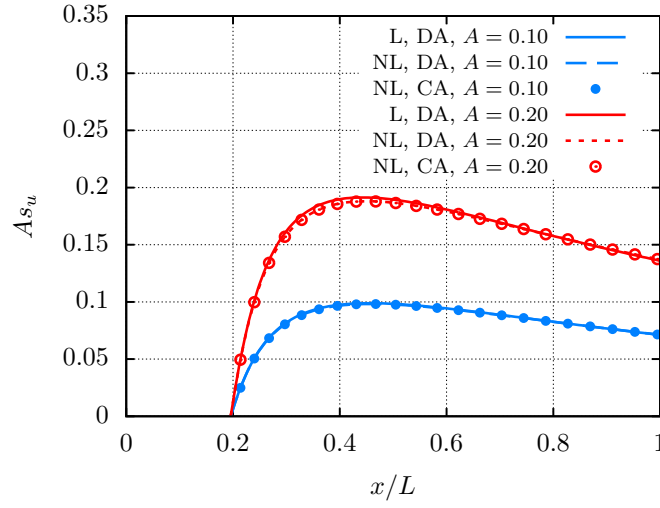


Figure 7. Evolution of streak amplitudes based on u , As_u , of linear (L) and nonlinear (NL) optimal perturbations initialized at $x_0/L = 0.1957$ with $m = 50$ and $J = G_{mean}$. Results based on the continuous adjoint (CA) and on the discrete adjoint (DA) approaches are included for comparison.

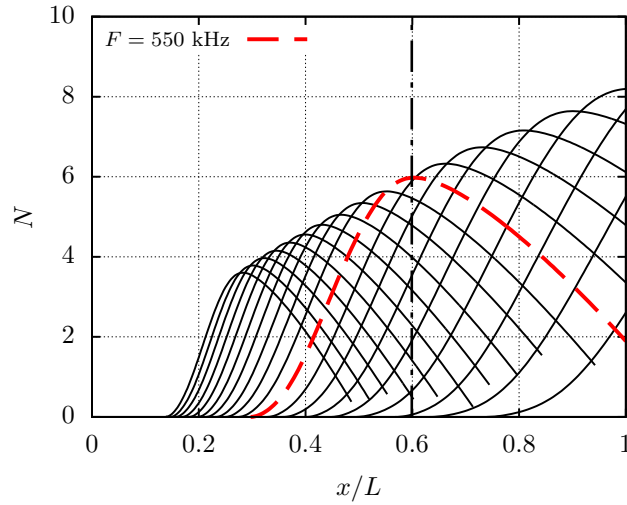


Figure 8. N -factors of planar second mode disturbances in an unperturbed Mach 6 circular cone boundary layer. The frequency is varied from $F = 350$ kHz to 800 kHz. The thick red dashed line denotes the frequency that first reaches $N = 6$ ($F = 550$ kHz). The vertical black dot-dashed line denotes the measured transition location.²²

are plotted for three different families of modes: mode MM_0 reduces to a 2D Mack mode disturbance in the limit of $A \rightarrow 0$, whereas modes $MM_{1,V}$ and $MM_{1,S}$ correspond to oblique Mack mode disturbances (with fundamental azimuthal wavelength equal to streak spacing) of varicose and sinuous type, respectively. Mode shapes for each family at frequencies corresponding to peak local growth rate are shown in Figs. 9(b) through 9(d) for a streak amplitude of $A = 0.10$. Figure 9(a) shows a progressive reduction in the peak growth rate of MM_0 modes with increasing streak amplitude, although the rate of decrease becomes smaller at higher values of A . The growth rate curves are displaced toward lower frequencies because the MM_0 mode shape concentrates on the crests of the modified flow (i.e., regions of increased boundary layer thickness) as shown by Fig. 9(b). Also, Fig. 9(a) shows the opposite effect for the $MM_{1,V}$ modes, which are strongest within the valleys of the modified basic state (Fig. 9(c)). The growth rates of the $MM_{1,V}$ modes increase with streak amplitude up to $A = 0.10$, and then decrease at higher A . In this case, the peak growth frequencies increase with A . The upper neutral frequency also increases with A while the lower neutral frequency remains relatively unchanged, leading to a higher bandwidth of unstable modes at larger A . In contrast, the streaks have a stabilizing influence on the $MM_{1,S}$ modes for all A (Fig. 9(a)), and similar to the MM_0 modes, their peak growth frequency is reduced as a consequence of their mode shapes distribution that peaks in the neighborhood of the crests (Fig. 9(d)).

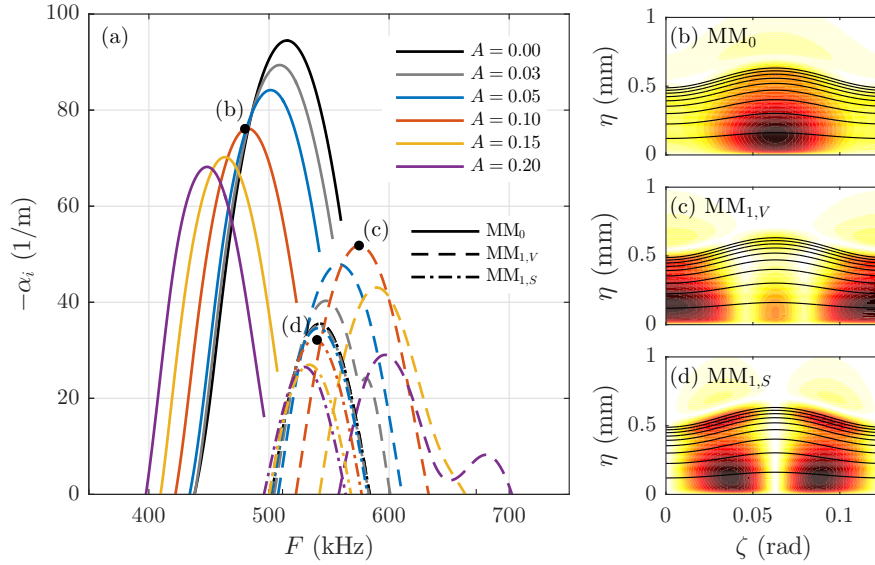


Figure 9. (a) Spatial growth rates ($-\alpha_i$) of planar Mack modes (MM_0) and oblique Mack modes with varicose ($MM_{1,V}$) and sinuous ($MM_{1,S}$) mode shapes for selected streak amplitudes at $x/L = 0.5$. Also, isocontours of streamwise velocity magnitude for $A = 0.10$ and frequencies (b) $F = 480$ kHz for MM_0 , (c) $F = 575$ kHz for $MM_{1,V}$, and (d) $F = 540$ kHz for $MM_{1,S}$. The color map of (b,c,d) varies from $|\hat{u}| = 0$ (light yellow) to $|\hat{u}| = 1$ (dark red). The isolines of basic state massflux, $\bar{p}\bar{u} = 0 : 0.1 : 0.9$, are added for reference.

To characterize the overall effect of streaks on the amplification of a Mack mode disturbance, we now examine the spatial evolution of a fixed frequency MM_0 mode with the plane-marching PSE. The logarithmic amplification ratio based on the energy norm of Eq. 10 is used as a measure of the disturbance amplification. Figure 10(a) illustrates the N -factor evolution of the MM_0 mode with frequency $F = 550$ kHz for the unperturbed basic state ($A = 0.00$) and the streaky flow with $A = 0.10$, together with the mode shape at three axial positions ($x/L = 0.40, 0.55$, and 0.70 for the $A = 0.10$ case in Figs. 10(b) through 10(d), respectively). The maximum value of the N -factor is $N = 4.8$ for the perturbed case and $N = 6.0$ for the unperturbed case. Furthermore, the location of peak N -factor is moved downstream from $x/L = 0.6$ to $x/L = 0.7$. The N -factor evolution for the perturbed case also indicates a different growth rate behavior in comparison with the unperturbed case. As the streak amplitude increases to its maximum value near $x/L = 0.55$ (Fig. 6(a)), the N -factor for the $A = 0.10$ case progressively deviates from that in the unperturbed case because of a lower amplification rate; however, following a local N -factor peak near $x/L = 0.55$, there is an additional region of amplification that causes the N -factor to increase again to reach its overall maximum near $x/L = 0.7$. The accompanying evolution of the mode shape in Figs. 10(b) through 10(d) shows that the peak of the fluctuation is initially located in the crest of the modified flow and then develops a secondary peak in the valley region that eventually becomes the location of dominant fluctuations. Comparison of this

mode shape evolution with the local results at $x/L = 0.5$ (Fig. 9) reveals that the MM_0 mode gradually evolves into the $MM_{1,V}$ mode downstream. The dashed lines in Fig. 10(a) indicate the N -factor evolution for the same frequency using two “artificial” basic states: a two-dimensional basic state corresponding to the spanwise average of the $A = 0.10$ flow, which corresponds to the unperturbed flow ($A = 0.00$) plus the mean flow distortion (MFD) due to the streak, and the perturbed flow with $A = 0.10$ minus the MFD of the perturbation. These extra cases are introduced to understand the primary mechanism for the effect of the streak on the reduced amplification of the MM_0 mode. By comparing the N -factor of the first extra case ($A = 0.00 + \text{MFD}$) with that for the unperturbed flow ($A = 0.00$), we can see that the MFD has a strong stabilizing influence on the MM_0 mode. The N -factor evolution for the second “artificial” case ($A = 0.10 - \text{MFD}$) indicates a longer region of amplification relative to the baseline case ($A = 0.00$), revealing the previously discussed downstream shift of the N -factor maximum for the total perturbed flow ($A = 0.10$) to be the result of the azimuthal gradients of the modified flow.

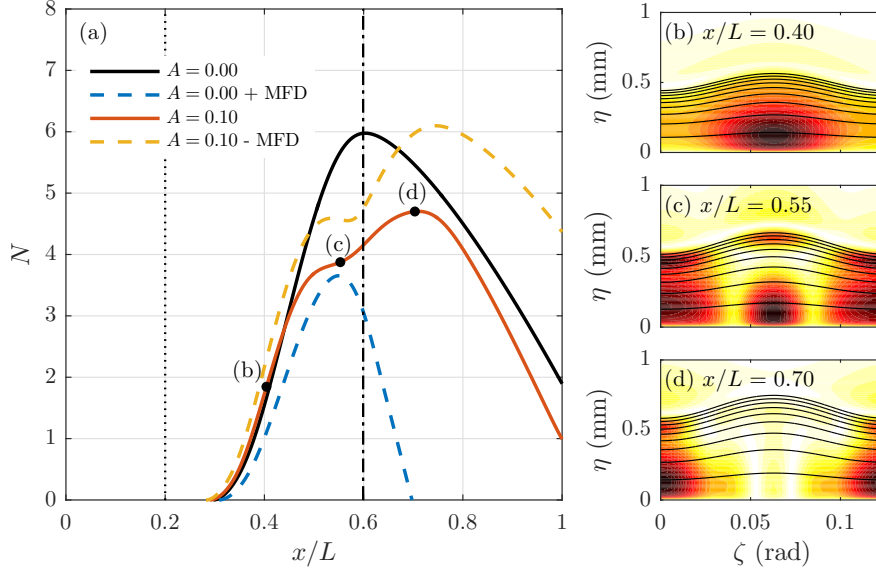


Figure 10. (a) Evolution of N -factors with frequency $F = 550$ kHz for the unperturbed basic state ($A = 0.00$), the unperturbed basic state plus the MFD of the $A = 0.10$ perturbation ($A = 0.00 + \text{MFD}$), the perturbed basic state ($A = 0.10$), and the perturbed basic state without the MFD ($A = 0.10 - \text{MFD}$). The vertical dotted line denotes the initial streak location, and the dash-dotted line denotes the experimentally observed transition location. Also, isocontours of streamwise velocity magnitude for $A = 0.10$ and positions (b) $x/L = 0.40$, (c) $x/L = 0.55$, and (d) $x/L = 0.70$. The color map of (b,c,d) same as Figs. 9(b)–9(d). The isolines of basic state massflux, $\bar{p}\bar{u} = 0 : 0.1 : 0.9$, are added for reference.

The overall effect of the streaks is summarized in Fig. 11, where the N -factor envelope of the MM_0 modes is plotted for each selected value of A . The primary focus of this work corresponds to the stabilizing effect of streaks on Mack mode disturbances, which have been shown to cause transition in the present flow configuration.²² For the conditions of the experiment,²² transition onset in the unperturbed cone boundary layer was measured to occur near $x_{tr}/L = 0.6$, where the peak N -factor of the MM_0 modes is $N = 6$. Selecting this value as the transition threshold, Fig. 11 shows how the transition onset due to MM_0 modes would be displaced downstream by the introduction of the optimal streaks. For the highest streak amplitude considered herein ($A = 0.20$), the MM_0 modes cannot reach the threshold N -factor over the entire length of the cone.

Due to the myriad paths to transition, however, the reduced growth of Mack modes becomes a “necessary” but not “sufficient” condition for delaying the onset of transition. In particular, oblique first-mode disturbances may come into play at the typical conditions of wind tunnel experiments at Mach 6. Indeed, calculations show that oblique sinuous first-mode disturbances with a subharmonic wavenumber of one half the streak wavenumber (denoted as $FM_{1/2,S}$) are destabilized by the streaks and, therefore, may reduce the extent of transition delay. Therefore, N -factor envelopes for the $FM_{1/2,S}$ modes at the selected streak amplitudes are also shown in Fig. 11. Observe that for streak amplitudes up to $A = 0.10$, the N -factor envelope of the MM_0 modes lies above the envelope of the $FM_{1/2,S}$ modes. But for $A = 0.15$ and $A = 0.20$, the $FM_{1/2,S}$ modes eventually overtake the MM_0 modes. Between the latter two cases, the threshold N -factor of $N = 6$ is reached further upstream for $A = 0.20$ ($x_{tr}/L = 0.92$), so the optimal streak amplitude for the present

flow configuration is close to $A = 0.15$, which reaches $N = 6$ at $x_{tr}/L = 0.96$, yielding a 60% increase in the length of the laminar flow relative to the unperturbed case.

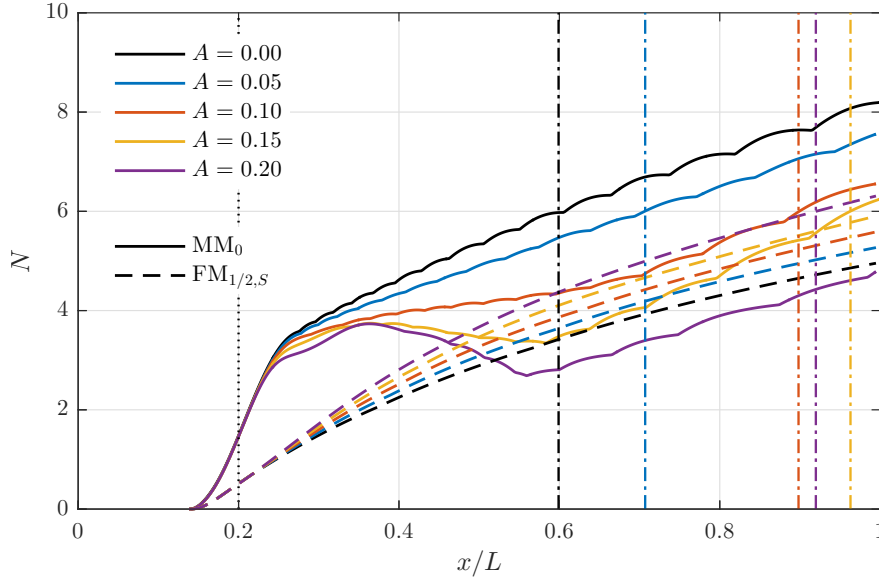


Figure 11. N-factor envelopes for nominally 2D Mack mode disturbances (mode MM_0 , solid lines) with a frequency range $F \in [350, 800]$ kHz and sinuous modes originating from first-mode waves with one half the azimuthal wavenumber of underlying streaks (mode $FM_{1/2,S}$, dashed lines) with a frequency range $F \in [50, 150]$ kHz. The vertical dotted line denotes the initial streak location, the black dash-dotted line denotes the experimentally observed transition location, and the colored dash-dotted lines denote the location where $N = 6$ is reached for each corresponding streak amplitude.

Finally, the effect of using nonlinearly optimal initial disturbances on the modal instability characteristics is investigated. Here, the streaks corresponding to $J = G_{mean}$ and finite-amplitude linear and nonlinear optimal disturbances from Fig. 7 are used as the basic state for instability evolution based on the plane-marching PSE. Figures 12(a) and 12(b) show the N -factor evolution of the planar Mack mode (MM_0) with $F = 550$ kHz and the subharmonic first mode ($FM_{1/2,S}$) with $F = 125$ kHz, respectively. A small difference is observed between the N -factor curves based on the linear and nonlinear optimal perturbations with $A = 0.10$ for both MM_0 and $FM_{1/2,S}$. The deviation is more visible at the higher streak amplitude of $A = 0.20$. For the planar Mack mode with $F = 550$ kHz, Fig. 12(a) shows a reduction of the first local maximum at $x/L \approx 0.46$ from $N = 2.6$ with the linear optimal perturbation to $N = 2.4$ with the nonlinear optimal perturbation. However, the second local maximum at $x/L \approx 0.8$ is unaffected by the initial disturbance selection and remains approximately equal to $N = 2.5$. For the subharmonic first mode with $F = 125$ kHz, the N -factor values associated with the nonlinear optimal disturbance are lower than those associated with the linear optimal disturbance with the same initial amplitude. The maximum N -factor at the end of the cone is reduced by $\Delta N \approx 0.25$.

We note that for streak amplitudes sufficiently higher than $A = 0.20$, the subharmonic first-mode disturbances evolve into highly unstable streak instabilities that eventually reverse the transition delay and become the agent for bypass transition.^{20,21} Of course, due to the lower surface temperature at typical flight conditions, the role of these first-mode waves diminishes in flight, implying that the streaks are likely to be even more effective in delaying transition on flight vehicles. Nonetheless, the computations presented in this work suggest that the effect of streaks on the onset of transition can be verified even under wind tunnel conditions. Prior to that, however, a thorough parameter study is desirable to address the effects of detuned disturbances and of potentially suboptimal streak profiles that are more readily realizable via the available set of actuation techniques. A parameter study for additional streak wavenumbers and excitation locations would also help with identifying the optimal flow control settings to maximize the transition delay for a given flow configuration.

V. Conclusions

Linear and nonlinear optimal transient growth analysis based on parabolized stability equations (PSE) have been conducted for the laminar flow based on the solution of the Navier-Stokes equations over a hy-

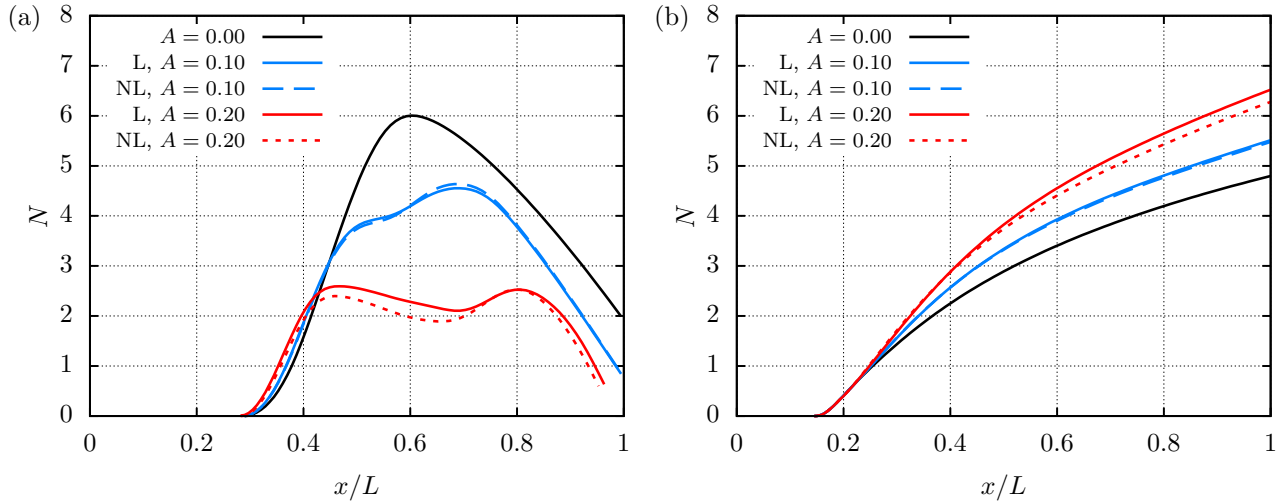


Figure 12. Evolution of N-factors associated to (a) MM_0 with $F = 550$ kHz and (b) $FM_{1/2,S}$ with $F = 125$ kHz for the unperturbed basic state ($A = 0.00$) and the perturbed basic states with linear (L) and nonlinear (NL) optimal perturbations with initial amplitudes corresponding to $A = 0.10$ and $A = 0.20$.

personic, 7° half-angle circular cone, boundary layer at Mach 6. Optimal growth computations based on the outlet energy gain and the mean energy gain are validated against the literature for the incompressible, zero-pressure-gradient, flat plate boundary layer. Furthermore, linear and nonlinear transient growth results are cross-validated by using the continuous and discrete adjoint approaches. The agreement is excellent in all cases. Furthermore, the plane-marching PSE have been used to monitor the nonlinear disturbance evolution of finite-amplitude linear and nonlinear optimal perturbations. Subsequently, the linear stability characteristics of the perturbed streaky boundary layer flow are studied using the linear form of the plane-marching PSE. The present results have demonstrated that stationary streaks in a Mach 6 axisymmetric flow over a cone reduce the peak amplification of boundary layer instabilities, suggesting a delay in the onset of laminar turbulent transition. For large streak amplitudes, the transition threshold is not reached by originally-dominant Mack mode instabilities, however, subharmonic first-mode waves that are destabilized by the streaks can limit the extent of transition delay. Setting the same initial amplitude for the linear and nonlinear optimal perturbations, the planar Mack mode and the subharmonic first-mode instabilities experience a lower amplification with the nonlinear optimal perturbation than with the linear optimal perturbation.

Acknowledgments

This research was sponsored by the NASA Transformational Tools and Technologies (TTT) Project of the Transformative Aeronautics Concepts Program under the Aeronautics Research Mission Directorate. A portion of the computational resources supporting this work were provided by the NASA High-End Computing (HEC) Program through the NASA Advanced Supercomputing (NAS) Division at Ames Research Center.

References

- ¹Mack, L., “Boundary layer linear stability theory,” *AGARD-R-709 Special course on stability and transition of laminar flow*, 1984, pp. 3.1–3.81.
- ²Klebanoff, P., “Effect of free-stream turbulence on the laminar boundary layer,” *Bull. Am. Phys. Soc.*, Vol. 10, p. 1323, 1971.
- ³Andersson, P., Brandt, L., Bottaro, A., and Henningson, D., “On the breakdown of boundary layer streaks,” *J. Fluid Mech.*, Vol. 428, 2001, pp. 29–60.
- ⁴Boiko, A., Westin, K., Klingmann, B., Kozlov, V., and Alfredsson, P., “Experiments in a boundary layer subjected to free stream turbulence. Part 2. The role of TS-waves in the transition process,” *J. Fluid Mech.*, Vol. 281, 1994, pp. 219–245.
- ⁵Cossu, C. and Brandt, L., “Stabilization of Tollmien-Schlichting waves by finite amplitude optimal streaks in the Blasius boundary layer,” *Phys. Fluids*, Vol. 14, No. 8, 2002, pp. L57–L60.
- ⁶Bagheri, S. and Hanifi, A., “The stabilizing effect of streaks on Tollmien-Schlichting and oblique waves: a parametric study,” *Phys. Fluids*, Vol. 19, 2007, pp. 078103–1–078103–4.

- ⁷Fransson, J., Talamelli, A., Brandt, L., and Cossu, C., “Delaying transition to turbulence by a passive mechanism,” *Phys. Rev. Lett.*, Vol. 96, 2006, pp. 064501.
- ⁸Shahinfar, S., Sattarzadeh, S., Fransson, J., and Talamelli, A., “Revival of classical vortex generators now for transition delay,” *Phys. Rev. Lett.*, Vol. 109, 2012, pp. 074501.
- ⁹James, C., “Boundary-layer transition on hollow cylinders in supersonic free flight as affected by Mach number and a screwthread type of surface roughness,” NASA TR-Memo-1-20-59A, 1959.
- ¹⁰Fujii, K., “Experiment of the two-dimensional roughness effect of hypersonic boundary-layer transition,” *J. Spacecraft Rockets*, Vol. 43, No. 4, 2006, pp. 731–738.
- ¹¹Fong, K., Wang, X., and Zhong, X., “Numerical simulation of roughness effect on the stability of a hypersonic boundary layer,” *Comput. Fluids*, Vol. 96, 2014, pp. 350–367.
- ¹²Fong, K., Wang, X., Huang, Y., Zhong, X., McKiernan, G., Fisher, R., and Schneider, S., “Second mode suppression in hypersonic boundary layer by roughness: design and experiments,” *AIAA J.*, Vol. 53, No. 10, 2015, pp. 3138–3143.
- ¹³Holloway, P. and Sterrett, J., “Effect of controlled surface roughness on boundary-layer transition and heat transfer at Mach number of 4.8 and 6.0,” NASA TR-D-2054, 1964.
- ¹⁴Choudhari, M., Li, F., and Edwards, J., “Stability analysis of roughness array wake in a high-speed boundary layer,” AIAA Paper 2009-0170, 2009.
- ¹⁵Li, F., Choudhari, M., Chang, C.-L., Greene, P., and Wu, M., “Development and breakdown of Gortler vortices in high speed boundary layers,” AIAA Paper 2010-0705, 2010.
- ¹⁶Li, F., Choudhari, M., Paredes, P., and Duan, L., “Secondary instability of stationary crossflow vortices in Mach 6 boundary layer over a circular cone,” NASA TM-2015-218997, 2015.
- ¹⁷Ren, J., Fu, S., and Hanifi, A., “Stabilization of the hypersonic boundary layer by finite-amplitude streaks,” *Phys. Fluids*, Vol. 28, 2016, pp. 024110–1–16.
- ¹⁸Paredes, P., Choudhari, M., and Li, F., “Transition delay in hypersonic boundary layers via optimal perturbations,” NASA TM-2016-219210, 2016.
- ¹⁹Schmid, P. J., “Nonmodal stability theory,” *Annu. Rev. Fluid Mech.*, Vol. 39, 2007, pp. 129–162.
- ²⁰Paredes, P., Choudhari, M., and Li, F., “Bypass transition in a supersonic flat plate boundary layer,” *Phys. Rev. Fluids*, Vol. 1, 2016, pp. 083601.
- ²¹Paredes, P., Choudhari, M., and Li, F., “Nonlinear transient growth and boundary layer transition,” AIAA Paper, 2016-3956, 2016.
- ²²Grossir, G., Musutti, D., and Chazot, O., “Flow characterization and boundary layer transition studies in VKI hypersonic facilities,” AIAA Paper 2015-0578, 2015.
- ²³Pralits, J., Airiau, C., Hanifi, A., and Henningson, D., “Sensitivity analysis using adjoint parabolized stability equations for compressible flows,” *Flow Turbul. Combust.*, Vol. 65, 2000, pp. 183–210.
- ²⁴Paredes, P., Choudhari, M., Li, F., and Chang, C.-L., “Optimal growth in hypersonic boundary layers,” *AIAA J.*, Vol. 54, No. 10, 2016, pp. 3050–3061.
- ²⁵Tempelmann, D., Hanifi, A., and Henningson, D., “Spatial optimal growth in three-dimensional boundary layers,” *J. Fluid Mech.*, Vol. 646, 2010, pp. 5–37.
- ²⁶Mack, L. M., “Boundary Layer Stability Theory,” Tech. Rep. 900-277, Jet Propulsion Lab., Pasadena, CA, 1969.
- ²⁷Hanifi, A., Schmid, P., and Henningson, D., “Transient growth in compressible boundary layer flow,” *Phys. Fluids*, Vol. 8, 1996, pp. 51–65.
- ²⁸Tumin, A. and Reshotko, E., “Optimal disturbances in compressible boundary layers,” *AIAA J.*, Vol. 41, 2003, pp. 2357–2363.
- ²⁹Zuccher, S., Tumin, A., and Reshotko, E., “Parabolic approach to optimal perturbations in compressible boundary layers,” *J. Fluid Mech.*, Vol. 556, 2006, pp. 189–216.
- ³⁰Paredes, P., Hanifi, A., Theofilis, V., and Henningson, D., “The nonlinear PSE-3D concept for transition prediction in flows with a single slowly-varying spatial direction,” *Procedia IUTAM*, Vol. 14C, 2015, pp. 35–44.
- ³¹Paredes, P., *Advances in global instability computations: from incompressible to hypersonic flow*, Ph.D. thesis, Universidad Politécnica de Madrid, 2014.
- ³²Zuccher, S., Bottaro, A., and Luchini, P., “Algebraic growth in a Blasius boundary layer: Nonlinear optimal disturbances,” *Eur. J. Mech. B Fluids*, Vol. 25, 2006, pp. 1–17.
- ³³Hermanns, M. and Hernández, J. A., “Stable high-order finite-difference methods based on non-uniform grid point distributions,” *Int. J. Numer. Meth. Fluids*, Vol. 56, 2008, pp. 233–255.
- ³⁴Paredes, P., Hermanns, M., Le Clainche, S., and Theofilis, V., “Order 10^4 speedup in global linear instability analysis using matrix formation,” *Comput. Meth. Appl. Mech. Eng.*, Vol. 253, 2013, pp. 287–304.
- ³⁵Paredes, P., Choudhari, M., Li, F., and Chang, C., “Transient growth analysis of compressible boundary layers with parabolized stability equations,” AIAA Paper (to appear), 2016.
- ³⁶Andersson, P., Berggren, M., and Henningson, D., “Optimal disturbances and bypass transition in boundary layers,” *Phys. Fluids*, Vol. 11, 1999, pp. 134–150.
- ³⁷Paredes, P., Choudhari, M., and Li, F., “On blunt-body paradox and transient growth on a hypersonic spherical forebody,” *Phys. Rev. Fluids*, Vol. to appear, 2017.